RSC Advances

PAPER

View Article Online
View Journal | View Issue



Cite this: *RSC Adv.*, 2026, **16**, 155

# Ammonium "catch and release" from wastewater using TEMPO-oxidized cellulose nanofiber beads

Yusleny Ramirez-Tarazona, Luz Amelia Calderón-Vergara, Cristian Blanco-Tirado and Marianny Y. Combariza *

Domestic wastewater is increasingly recognized as a valuable resource for nutrient recovery. This study presents the development of biodegradable nanocellulose-based beads synthesized from palm oil empty fruit bunches (EFB) for the recovery and reuse of ammonium. TEMPO-oxidized cellulose nanofibers (TOCN) were produced *via* a one-step oxidation process and shaped into beads through sodium-ion-mediated ionotropic gelation. The resulting TOCN beads (TOCNB) exhibited a high ammonium adsorption capacity of 30.30 mg $g^{-1}$, governed by a combination of physisorption and electrostatic interactions. Adsorption kinetics followed a pseudo-first-order model, while equilibrium data were best described by the Langmuir isotherm, indicating monolayer adsorption. The adsorption performance was significantly influenced by pH, ionic strength, and contact time, with optimal uptake observed at pH 8. Competitive ion experiments revealed that $K^+$ and $SO_4^{2-}$ notably reduced ammonium adsorption, while $Ca^{2+}$ had a lesser effect due to steric hindrance. Germination assays with *Phaseolus vulgaris* demonstrated that TOCNB–$NH_4^+$ enhanced seedling growth to a comparable extent as commercial urea, confirming its potential as a controlled-release biofertilizer. These findings highlight TOCNB as a sustainable material for nutrient recovery and agricultural reuse, aligning with circular economy principles.

Received 24th October 2025
Accepted 5th December 2025

DOI: 10.1039/d5ra08174b

rsc.li/rsc-advances



## 1 Introduction

The rapid growth of the population and industrial development has led to a significant increase in wastewater discharges, which contain pollutants from both natural and anthropogenic sources, thereby jeopardizing the availability of clean water.[1] Among these pollutants are critical nutrients such as nitrogen (N) and phosphorus (P), which, if allowed to accumulate, can cause eutrophication of aquatic ecosystems. Paradoxically, the depletion of these very nutrients—particularly phosphorus—is raising concern due to their essential roles in agricultural fertilization.[2] As global demand for these finite resources continues to escalate, addressing their pollution and depletion simultaneously becomes increasingly critical for sustainable ecosystem management and food security.

Various strategies have been explored for ammonium recovery from wastewater, encompassing biological and physicochemical treatments. Biological techniques include nitrification, denitrification, anammox, and membrane bioreactors. In contrast, physicochemical methods involve chemical precipitation, ion exchange, membrane filtration, and adsorption.[3,4] Among these methods, adsorption stands out due to its high removal efficiency, cost-effectiveness, and operational simplicity. This method is particularly advantageous for treating nutrient low-concentration effluents, such as municipal wastewater, where ammonium concentrations typically average around 100 mg per L $NH_4$–N.[5] Nutrient adsorption from wastewater occurs through physical and chemical mechanisms that depend on interactions between the adsorbate and the adsorbent surface.[4] Physisorption, driven by van der Waals forces, is typically reversible and allows for multilayer adsorption.[6] In contrast, chemisorption involves the formation of chemical bonds, such as covalent or ionic interactions, resulting in stronger, more selective adsorption.[7] Additionally, hybrid mechanisms such as ion exchange, porosity trapping, and π–π interactions may also play a role in adsorption efficiency.[8]

Common adsorbents include biochar, activated carbon, and zeolites.[9] However, recently, innovative materials such as hydrogels—three-dimensional polymeric networks—have attracted attention for their superior adsorption capacity. This is attributed to the ease with which solutes diffuse through the gel structure.[10–16] To improve the sustainability and cost-effectiveness of hydrogel materials, growing attention has been directed toward biopolymer-based systems derived from agricultural residues. Among these, palm oil Empty Fruit Bunches (EFB) represent a particularly promising feedstock. EFB is the most abundant solid by-product of palm oil extraction, accounting for approximately 21% of the fresh fruit bunch and contributing to an annual global production exceeding 68 million tonnes.[17] Its potential lies in its rich lignocellulosic composition—typically comprising about 50% cellulose, 25%

*Escuela de Química, Universidad Industrial de Santander, Bucaramanga, 680002, Colombia. E-mail: marianny@uis.edu.co*

lignin, and 15% hemicellulose[18]—which makes it an attractive raw material for the development of renewable and functional biopolymers. Using EFB as a raw material for hydrogel production not only adds value to an otherwise underutilized residue but also aligns with the growing demand for sustainable, economically viable materials.

Polymer-based adsorbents, such as cellulose, are emerging as promising materials for various applications due to their biodegradability, biocompatibility, widespread availability, and cost-effectiveness. However, the dense, compact structure inherent to native cellulose significantly restricts the accessibility of active sites, thereby reducing adsorption capacity. To address this limitation, researchers have turned to both chemical and mechanical modifications. Mechanical treatments, including microfibrillation and nanofibrillation, effectively disrupt hydrogen bonding and van der Waals interactions within cellulose's crystalline regions. This disruption not only enhances the surface area but also increases the availability of hydroxyl groups, thereby improving the adsorption potential of cellulose-based adsorbents. Meanwhile, TEMPO-mediated oxidation (using 2,2,6,6-tetramethylpiperidine-1-oxyl) selectively converts primary hydroxyl groups at the C6 position into carboxylate groups. This modification imparts negative charges to the cellulose surface, boosting adsorption through electrostatic attraction. The process typically employs sodium hypochlorite (NaClO) as the primary oxidant, TEMPO as a catalyst, and sodium bromide (NaBr) as a co-oxidant in an alkaline environment. It affects both crystalline and amorphous regions, aiding fiber defibrillation and decreasing agglomeration. The synergy of mechanical and chemical treatments produces TEMPO-oxidized cellulose nanofibers (TOCN) with markedly enhanced adsorption capabilities.[19]

Previous studies on TOCN show that these fibers exhibit nanometer-scale diameters, micrometer-scale lengths, and high surface charge.[20,21] These properties enable them to act as flexible colloidal particles with a high aspect ratio, capable of interacting, deforming, and entangling.[22] In aqueous suspension, the homogeneous dispersion of TOCN can be converted into a gel using several strategies, including lowering the pH or increasing the salt concentration beyond a critical point.[20] In particular, the gelation process induced by adding salts such as $CaCl_2$ or NaCl, in which cations move from the external saline solution into the polymeric solution, is known as sodium/calcium ion-mediated external ionotropic gelation (IG).[23,24] During this process, calcium or sodium ions diffuse through the polymer dispersion, triggering cross-linking and gel formation. For TOCN, coagulation happens because adding salt decreases the Debye length of the fibrils, which lowers their electrostatic repulsion and encourages attractive forces like van der Waals interactions and hydrogen bonds.[25] Overall, the gelation and colloidal stability of nanocellulose-based gels produced by IG are governed by electrostatic interactions and the fibrillar network's ability to entangle, enabling the formation of three-dimensional structures as illustrated in Fig. 1.[26]

Cellulose nanofibers are used to create cellulose beads—spherical particles usually larger than 10 μm—that are widely

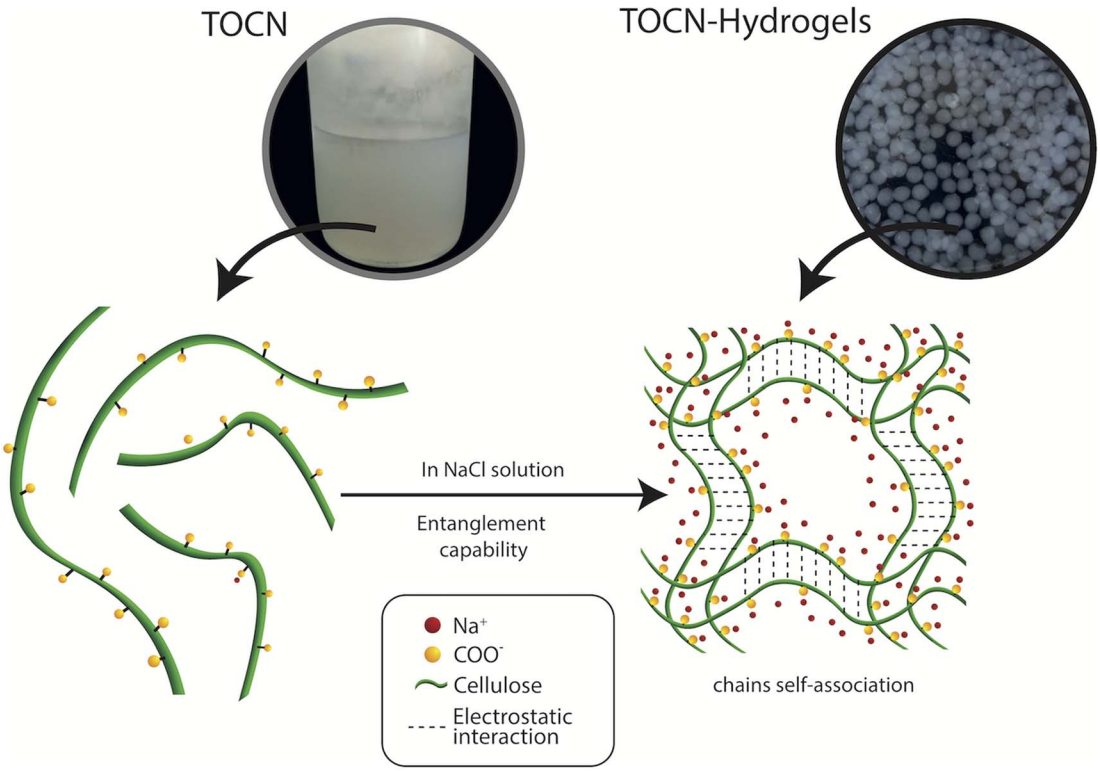


Fig. 1 Schematic illustration of TOCNs in aqueous suspension and in a 3D structure where networks form through physical gelation caused by chain self-association in the presence of salt (NaCl).

applied in chromatography, metal ion exchange, and water treatment.[27] Producing these beads typically involves three main steps: dissolving cellulose, shaping it into spheres, and regenerating the polysaccharide. The main differences in fabrication methods lie in the choice of solvent and particle formation technique. Standard methods include spraying, dripping or dropping, jet cutting, and spinning drop atomization, among others.[28–31] Recent studies on TEMPO-oxidized cellulose nanofiber (TOCN) beads demonstrate their vast potential in cell delivery, low-density lipoprotein (LDL) removal from blood, water purification, and heavy metal adsorption.[10,11,32–35] Nonetheless, their use in ammonium adsorption from wastewater and release for fertilization remains underexplored, offering a promising path toward sustainable materials in nutrient recycling.[36]

This work aims to demonstrate that novel TOCN-based beads, fabricated with cellulose extracted from empty fruit bunches (EFB) from the palm industry, can effectively adsorb ammonium from synthetic wastewater while also serving as a controlled-release biodegradable fertilizer in soils. To achieve this, carboxylated cellulose beads were prepared *via* a one-step TEMPO/NaClO/NaBr oxidation process, enhanced by ultrasound, followed by simple ionotropic gelation in a NaCl bath, yielding oval-shaped beads with ammonium adsorption capacity. The ammonium adsorption efficiency of these beads was evaluated in batch experiments to assess the effects of pH, ionic strength, and contact time on adsorption.

Characterization techniques such as Fourier transform infrared spectroscopy (FTIR) and scanning electron microscopy (SEM) were used to examine the surface chemistry, structure, porosity, and morphology of the beads. Mechanical, optical, gravimetric, and light scattering analyses helped assess their compressive strength, size, shape, weight, swelling ratio, and $\zeta$ potential. Additionally, conductivity titration was employed to determine the carboxylate active-site content and the oxidation level of the adsorbent surface. To understand the adsorption mechanisms, equilibrium isotherms and kinetics were analyzed. Finally, the performance of TOCN beads as fertilizers was tested in seed germination and growth tests in using quartz sand, providing valuable insights into their potential role in sustainable agricultural practices.

# 2 Experimental

## 2.1 Reagents and materials

Raw EFB (*Elaeis guineensis*) was supplied by the Central Palm Oil Extraction Plant in Puerto Wilches, Santander, Colombia. The chemical reagents used in the study include hydrogen peroxide ($H_2O_2$), sodium hydroxide (NaOH), hydrochloric acid (37% HCl), ethanol (analytical grade), sodium chloride (NaCl), and ammonium chloride ($NH_4Cl$), all sourced from Merck (Darmstadt, Germany). The TEMPO (2,2,6,6-tetramethylpiperidine-1-oxyl) radical was acquired from Sigma-Aldrich (Saint Louis, MO, USA). A commercial sodium hypochlorite solution (NaClO, 15%) was supplied by Suquín S.A.S (Bucaramanga, Colombia) and was standardized according to ASTM method D2022.

## 2.2 Fabrication of TEMPO-oxidized cellulose nanofibers beads (TOCNB)

The preparation of TEMPO-oxidized cellulose nanofibers (TOCN) followed a procedure previously established by our research team. Briefly, the raw EFB was delignified (EFB-AHP) using the method described by Ovalle-Serrano *et al.*[37] Subsequently, cellulose nanofibers were extracted using the TEMPO radical oxidation, as outlined by Martínez-Ramírez *et al.*[38] Finally, TOCN beads were coagulated by IG using the falling-ball method by Trygg *et al.*,[39] employing a 1 mL syringe pump with a 2 mm nozzle (IPS-12RS, 20 mL $h^{-1}$). The 1.48% w/v TOCN suspension was cooled to 0 °C and added dropwise, from a height of 1–2 cm, into a 10% NaCl coagulant bath cooled to 5 °C. The resulting TOCN beads were designated as TOCNB.

## 2.3 Materials characterization

The degree of oxidation (DO) and carboxylate content ($\sigma$) of TOCN were measured using conductimetry, following the method previously reported by Martínez-Ramírez *et al.*[38] Measurements were performed five times. Additionally, the zeta potential ($\zeta$) of TOCN (0.1% w/v) was measured using dynamic light scattering (DLS) with a MALVERN Zetasizer ZS90 instrument (Worcestershire, UK), using a DTS-1070 cell. The structures of EFB, EFB-AHP, TOCN film, and TOCNB samples were characterized with a Bruker Tensor 27 FT-IR spectrophotometer equipped with a Bruker A225/Q platinum ATR and a diamond crystal. IR spectra were recorded from 4000 to 200 $cm^{-1}$ at a resolution of 2 $cm^{-1}$, with a scan rate of 2.2 kHz and 32 scans. TOCN films and beads were made by drying suspensions at 60 °C for 24 hours. Spectra were plotted using OriginPro 2024.

The morphology of TOCNB was investigated using a scanning electron microscope (Thermo Fisher Scientific Scios 2 DualBeam) equipped with an EDX detector. An acceleration voltage of 15.00 kV was applied, and images were captured at magnifications ranging from 250× to 10 000×. TOCN monoliths were prepared by dripping 10% NaCl into 50 mL of TOCN. Both the monoliths and TOCNB underwent solvent exchange from water to acetone by gradually increasing the acetone concentration from 20% to 100%. The specimens were then dried with liquid nitrogen and lyophilized at −84 °C for 24 hours. TOCN, TOCN monoliths, beads, and their cross sections were coated with conductive carbon tape using a sputter coater before imaging.

The size and shape of the TOCNB were analyzed following the Trygg *et al.*[39] methods with minor modifications. Eighty-five wet beads were weighed and photographed. The beads were then dried at room temperature for 24 hours until constant weight. Images were processed to binary format for average size and shape determination, and the major and minor axes were obtained by fitting ellipses in Adobe Illustrator (version 29.3). For wet beads, compressive strength was determined with a dynamic mechanical analyzer (DMA Q800). A single compression test was performed with a preload force of $3 \times 10^{-4}$ N and a ramp force of 0.020 N $min^{-1}$ at 30 °C. Compressive stress was calculated based on the cross-sectional area at the equator. Measurements were conducted in quintuplicate. The

equilibrium swelling ratio (%ESR) was measured gravimetrically, as described by Pal and Banerjee.[40] Dry beads were weighed ($W_d$), soaked in distilled water at 37 °C for 72 hours, and blotted. The wet beads were weighed ($W_w$), and the %ESR calculation was performed according to the equation:

$$\%\mathrm{ESR} = \frac{(W_w - W_d)}{W_d} \times 100 \quad (1)$$

### 2.4 Adsorption tests

Adsorption of ammonium ions onto TOCNB was carried out through batch experiments to determine the adsorption kinetics rate and equilibrium isotherm. All experiments were conducted at 25 °C, pH 7, 150 rpm, with a dosage of 0.25 g per L TOCNB (dry weight) in a 100 mg per L $NH_4^+$ solution, unless otherwise stated. Ammonium concentrations were measured using UV-Vis spectroscopy at 690 nm. Kinetics experiments were conducted with time intervals from 10 to 60 minutes. TOCNB was added to an Erlenmeyer flask with the adsorbate ($NH_4^+$) and stirred at a constant temperature. The samples were filtered, and the resulting filtrate was analyzed to determine the residual concentrations of the adsorbate. The equation for calculating the adsorption capacity ($q_t$) is as follows:

$$q_t = \frac{(C_0 - C_e) \times V}{m} \quad (2)$$

where $C_0$ and $C_e$ are the initial and equilibrium molar concentration of the adsorbate solution (mg per L $NH_4^+$), respectively. $V$ is the volume of the adsorbate solution used (L), and $m$ is the weight (g) of the adsorbent.

Isotherm studies were performed at initial ammonium concentrations from 10 to 160 mg per L $NH_4^+$, with a contact time of 60 minutes. The isotherm studies were modelled using the Langmuir and the Freundlich models. Additionally, the effect of pH on the ammonium adsorption was evaluated over a pH range of 5 to 8, with adjustments made using 0.01 M NaOH and HCl solutions. To assess the impact of ionic strength, 0.25 g per L TOCNB (dry weight) was incubated for 60 minutes in the presence of 20 mg per L $K^+$, 20 mg per L $Ca^{2+}$, and 48 mg per L $SO_4^{2-}$ from KCl, $CaCl_2$, and $Na_2SO_4$.

### 2.5 Germination tests

Seed germination tests were performed to evaluate the potential of TOCNB as an ammonium fertilizer. Red bean (*Phaseolus vulgaris* L.) seeds were selected to examine TOCNB's influence on germination and seedling growth. The germination experiment involved using 500 g of clean white quartz sand ($SiO_2$) as a chemically inert substrate and control soil, and sand–urea mixtures containing 4.67 mg of $NH_4^+$, as well as sand–TOCNB mixtures that also contained 4.67 mg of $NH_4^+$ previously captured by the TOCNB from an aqueous stock solution. The three mixtures were placed in containers under identical conditions of sunlight (5.0–5.6 kWh per $m^2$ per day), humidity (85%), and temperature (22–24 °C). All experiments were performed in triplicate. After germination, seedling growth was measured by evaluating stem length, dry weight, and the number and length of leaves.

## 3 Results and discussion

### 3.1 TOCN and TOCN beads (TOCNB) characterization

The TOCN oxidation degree (OD) and carboxylic content ($\sigma$) were first assessed using conductimetry measurements. The OD and $\sigma$ of TOCN were 0.20 and 1.29 mmol $g^{-1}$, respectively (see Fig. S1, eqn (S1), and (S2)). This indicates that approximately 1.29 mmol of hydroxymethyl groups per gram of cellulose were converted into carboxylate groups during the oxidation process. These findings align with trends observed in EFB-AHP, oxidized oil palm lignocellulosic biomass, and other oxidized plant biomass matrices.[38,41–43] Additionally, the stability of aqueous suspensions of TOCN was mainly influenced by electrostatic repulsion between ionic groups on the surface of cellulose nanofibers. This was quantitatively evaluated by measuring the $\zeta$ potential, which serves as an indicator of colloidal dispersion stability.[44,45] Generally, a $\zeta$ potential of $\pm$40 mV or higher indicates electrostatic stabilization, preventing TOCN aggregation over time. Conversely, a $\zeta$ potential of ($\leq\pm$40 mV) indicates rapid coagulation due to attractive forces. The $\zeta$ potential for TOCN suspension was −51 mV, confirming stable aqueous dispersions of the material.[37,38,46]

Additionally, Fourier-transform infrared spectroscopy (FTIR) analysis was used to confirm the chemical structure and identify the functional groups in the cellulose nanofibers, verifying the success of the TEMPO oxidation process. Fig. S2 shows the FTIR spectra of EFB, EFB-AHP, TOCN, and TOCNB, all exhibiting characteristic cellulose peaks, including the C6–$H_2$ flexion (1317 $cm^{-1}$), the C–O–C stretching vibration of the pyranose ring skeleton (1159 $cm^{-1}$), C–O vibration (1033 $cm^{-1}$), and the vibration signal of C1–H (900 $cm^{-1}$). The peak around 3300 $cm^{-1}$ is attributed to O–H stretching vibrations.[47] After delignification (EFB-AHP sample), the absence of peaks associated with the typical vibrations of the C=O linkage of hemicelluloses (1733 $cm^{-1}$) and C–O–C vibrations (1238 $cm^{-1}$) of aromatic ether linkages in lignin indicates the effective removal of lignin and hemicellulose after $H_2O_2$ treatment.[48,49] Additionally, the FTIR spectra of TOCN and TOCNB exhibit a new peak at 1609 $cm^{-1}$, assigned to the stretching vibration of carboxylate C=O groups in TOCN, confirming the surface oxidation of cellulose. No significant differences were observed between the FTIR signals of TOCN and TOCNB.[50]

TEMPO oxidation yields cellulose nanofibrils with a high aspect ratio and negative surface charges due to carboxyl groups.[21] These groups are essential for TOCN stability in aqueous dispersions, hydrogel formation, and also the ammonium "catch and release" process discussed later. The length and flexibility of nanocellulose fibrils influence the formation of hydrogels. High-aspect-ratio TEMPO oxidized cellulose nanofibrils (TOCNs) exhibit extensive surface area and abundant carboxylate functionalities, enabling efficient ionic crosslinking and gelation at significantly lower concentrations compared to shorter microfibrils.[51] Longer fibrils with high aspect ratios promote entanglement and transient network formation, enabling gel-like behavior at relatively low concentrations, resulting in highly porous, three-dimensional

networks.[52] Small-angle neutron scattering studies reveal that the addition of multivalent cations significantly reduces the Kuhn length (a measure of fibril stiffness), thereby enhancing fibril bending and intra- and inter-fibrillar entanglement, intensifying cross-linking, and stabilizing the gel network.[53] This interplay between fibril length and flexibility governs mechanical integrity, porosity, and swelling behavior, highlighting the importance of nanocellulose dimensions and conformational adaptability in tailoring hydrogel properties.[51–53]

During bead formation by IG, the ionic strength gradient-from the NaCl coagulation bath to the TOCN droplets-causes diffusion of $Na^+$ ions into the TOCN, weakening the electrical double layer around the negatively charged TOCN in aqueous solution. This enables the formation of ionic bridges between carboxylates, which eventually overcome repulsive forces (Fig. 1), leading to TOCN aggregation and the beads shown in Fig. 1 and 2.[26] These beads have a highly porous structure, which is useful for various applications, including adsorption, bone tissue engineering and drug delivery.[11,54,55] The porosity arises from the nanofibrous network created during the coagulation process. This structure enhances water retention and promotes the formation of an interconnected three-dimensional matrix, whose pore size and distribution are influenced by ionic diffusion kinetics, coagulant salt concentration, and the density of carboxyl groups on the nanofibrils.[56] These factors also affect the absorption capacity and swelling degree, as well as the physical and morphological properties of TOCNBs.

Upon TOCN coagulation, the translucent TOCNBs were characterized following the method described by Trygg *et al.*[39] Optical imaging (Fig. 2a) revealed that the beads exhibited an elliptical shape, with an average major axis of 5.79 ± 0.34 mm and a minor axis of 4.94 ± 0.34 mm. Additionally, the average dry-bead weight was 52.71 ± 2.32 mg. Circularity was calculated using the equations proposed by Russ and Ramanujan, yielding an average circularity of 0.98 ± 0.01.[57,58] The elliptical geometry further enhances adsorption efficiency by promoting uniform radial diffusion of ammonium ions into the hydrogel matrix, as noted by Landreau *et al.*[59] Additionally, the well-defined three-dimensional structure facilitates the recovery of beads from treated water using simple methods, such as filtration, making these structures practical for both pilot-scale and real-world wastewater treatment applications.[3]

The TOCNBs were oven-dried at 30 °C until their weight became constant. The solid TOCN beads exhibited an average

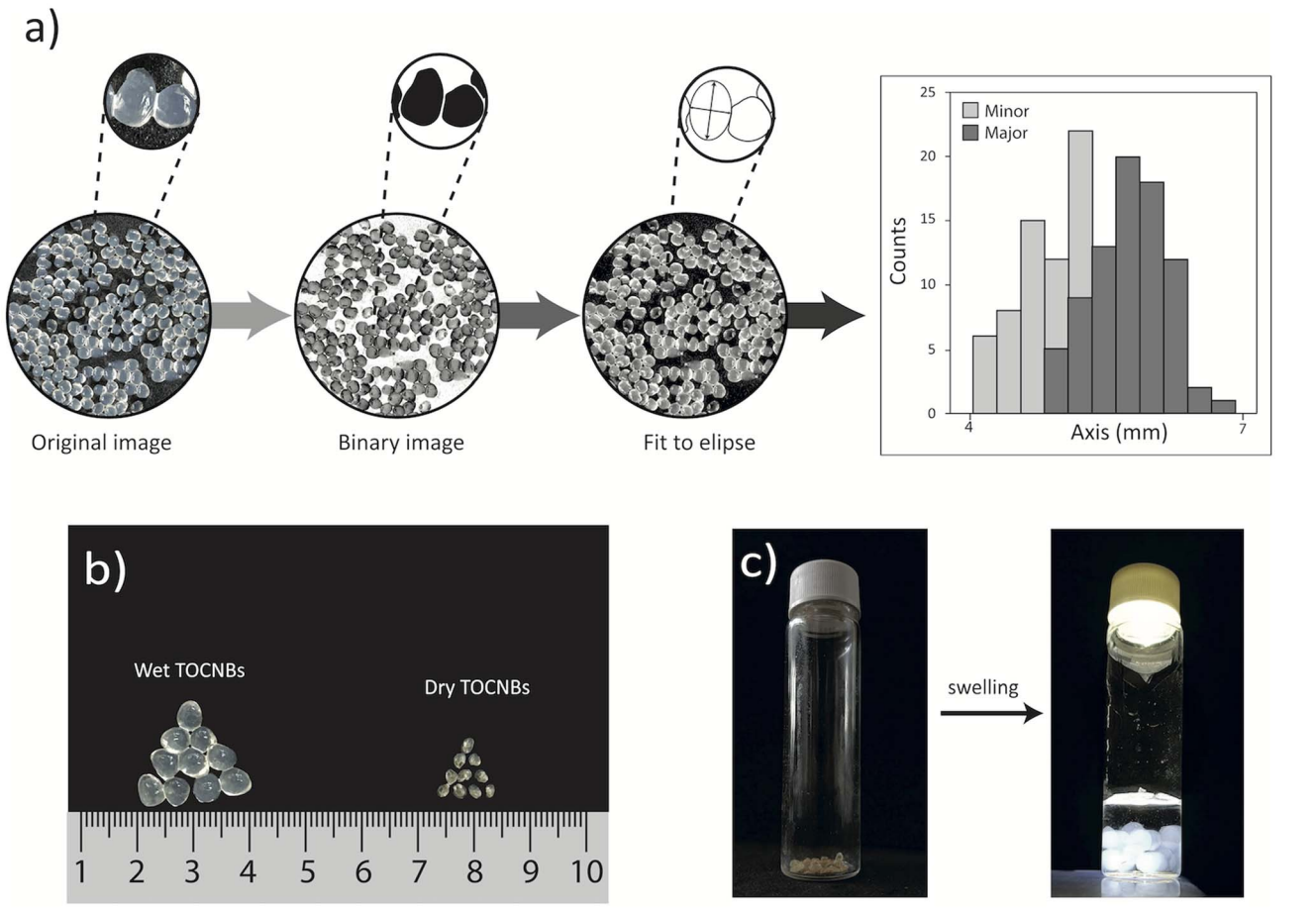


Fig. 2 (a) Size distribution and shape of TOCNB determined through image analysis (gray for minor axis, black for the major axis). (b) Digital images of TOCNB beads, showing wet and dry TOCNB after oven drying. (c) Digital images of solid TOCNB and after swelling. The concept for this figure was adapted from ref. 27 and 33.

diameter of 2.19 ± 0.18 mm and a dry weight of 2.19 ± 0.12 mg (Fig. 2b). Upon immersion in distilled water, they swelled to an average weight of 28.76 mg, demonstrating their high-water uptake capacity. However, after drying and subsequent rehydration, the beads showed partial recovery, indicating that the polymer network retained sufficient structural integrity to allow swelling, although the original hydrogel water content was not fully restored. The equilibrium swelling ratio (%ESR) was 1219 ± 1.56, confirming substantial water absorption despite the irreversible changes induced by drying. This swelling behavior aligns with previous research on beads made from oxidized nanocellulose.[56,60] The high %ESR is due to the hydrophilic nature of TOCN, which forms hydrogen bonds with water molecules, allowing the beads to absorb water and revert to their translucent hydrogel state.

Fig. 3 presents a stress–strain curve for TOCNBs showing an ultimate compressive strength of 1262.92 ± 62.876 Pa at a strain of 42 ± 0.6%, without breaking. Additionally, TOCNB has a compressive modulus of 11 kPa, indicating it is soft and easily deformable. This mechanical characteristic is common in hydrogels with high water content and low crosslinking density, aligning with the behavior of polymeric hydrogels.[61,62] Previous studies on hydrogels based on lignin-containing arabinoxylan and cellulose nanofibers reported a maximum compression of 50%.[63] The high deformability of TOCNB suggests high flexibility and a high water-absorption capacity, which could aid in ammonium diffusion within the polymer network. Furthermore, TOCNB maintained mechanical stability during manipulation in adsorption–desorption cycles. To increase maximum stress, adding crosslinking agents or using divalent cations during hydrogel synthesis are possible options.[64]

The structural features and elemental composition of the cellulose nanofibers TOCN and TOCNB were analyzed by scanning electron microscopy (SEM). Fig. 4a and b depict the surface of TOCN, while Fig. 4c and d show its surface and the cross-section of the TOCN monolith, respectively. Initially, as seen in Fig. 4a, the TOCN surface appears relatively smooth. However, at higher magnification (Fig. 4b), the fibers form an interconnected network of visible monofilaments with ridges and grooves. The network becomes increasingly textured and porous, with irregularities and protrusions. Meanwhile, the low-magnification SEM image shows the hydrogel's three-dimensional porous architecture (Fig. 4c), and the high-magnification image reveals the monolith's cross-section, where pores approximately hundreds of nanometers in size are visible. This porous structure influences the material's adsorption properties.[65]

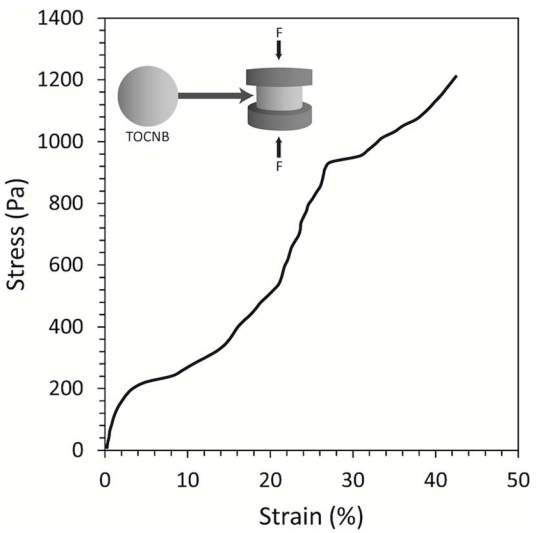


Fig. 3 Stress–strain curve derived from the compressive test of the TOCNB hydrogel.

### 3.2 Adsorption of ammonium by TOCNB

Multiple studies have established that TOCN possesses a p$K_a$ of approximately 4.0, a critical parameter that governs its cation-exchange behavior.[11,66,67] As pH rises above the p$K_a$, the carboxyl groups (–COOH) at the C6 position of the anhydroglucose units in TOCN gradually deprotonate, forming negatively charged carboxylate groups ($–COO^-$). Fig. 5a depicts TOCN's pH-responsive behavior, with green and yellow lines indicating the pH ranges where protonated and deprotonated carboxylic acids in TOCN dominate, respectively. At pH 7.4 and up, over 99.99% of COOH groups in TOCNs are deprotonated.[67] In contrast, at lower pH values, protonation reduces the TOCN surface charge density, weakening electrostatic interactions and diminishing cation uptake. This interpretation aligns with previous reports indicating that the zeta potential of TEMPO-oxidized cellulose nanofibers becomes more negative as pH increases, due to the gradual dissociation of surface carboxyl groups, and stabilizes near neutral pH once most acidic functionalities are dissociated.[68,69]

$NH_4^+$ ions in water are prevalent over a broad pH range (blue line in Fig. 5a), and only above pH > 9.2 neutral ammonia ($NH_3$) forms as indicated by the pink line in Fig. 5a.[70] Since $NH_4^+$ adsorption by TOCNB will involve electrostatic interactions, a theoretical effective pH range of 4 to 8 can be suggested for $NH_4^+$ uptake by the $–COO^-$ groups on cellulose beads. However, given that the pH of domestic wastewater in Colombia ranges from 5 to 8, we tested the effect of pH on the $NH_4^+$ adsorption capacity of TOCNB over that pH range.[71–73] Fig. 5a (black dotted line) shows that the $NH_4^+$ adsorption capacity of the beads steadily increases with rising pH, from 12.57 mg $g^{-1}$ at pH 5.0 to 40.32 mg $g^{-1}$ at pH 8.0. Adsorption increases by 3.2-fold over the pH range tested, as deprotonation enhances electrostatic attraction and promotes $NH_4^+$ retention by TOCNB.[74,75]

This pH-dependent behavior has profound implications for both wastewater treatment and agricultural reuse. On the one hand, ammonium capture by TOCNBs occurs under wastewater pH conditions, whereas in acidic soils (pH < 5.5), which are prevalent in tropical regions like Colombia,[76] the protonation of carboxylate groups could facilitate the desorption of previously adsorbed ammonium from TOCNBs. This release mechanism would be supported by the presence of competing cations such as $H^+$ and $Al^{3+}$ in soils, which could displace $NH_4^+$ from the bead matrix.[77] Because the carboxylate ion in TOCNB is the conjugate base of a weak acid, it will exchange an ammonium ion for

 

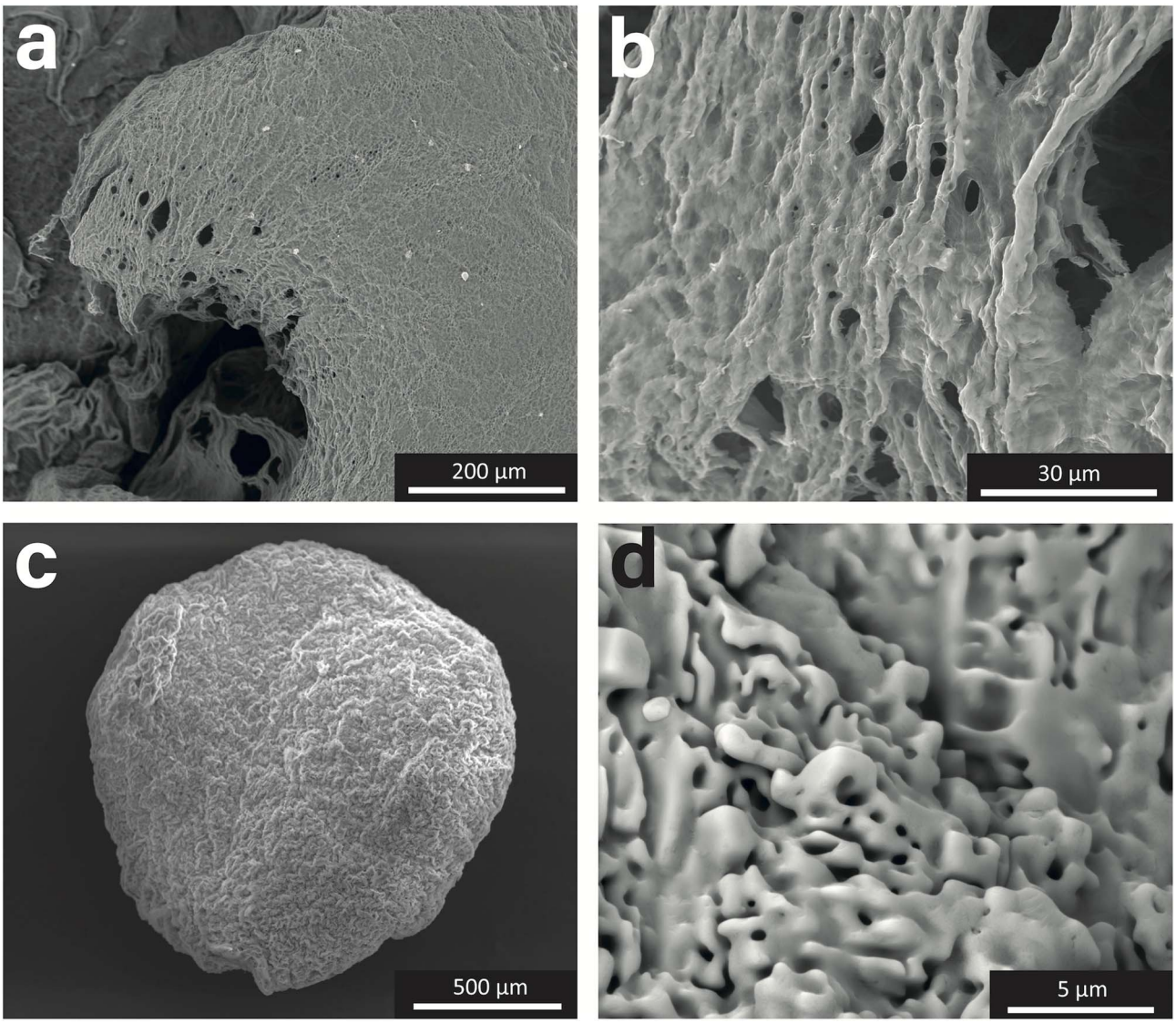


Fig. 4 FE-SEM images showing the surface morphology of (a) TOCN, (b) magnified view of TOCN, (c) TOCNB surface, and (d) cross-section of the TOCN monolith.

a proton. Therefore, TOCNB could serve as an efficient ammonium adsorbent for wastewater treatment and also act as a controlled-release fertilizer in acidic soils, helping to maintain nutrient levels and reduce leaching.[78]

In practical nutrient recovery applications, wastewater contains ions other than $NH_4^+$, such as $K^+$, $Ca^{2+}$, and $SO_4^{2-}$. These ions vary in concentration based on location and water source, whether domestic or industrial. To assess how these additional ions influence the $NH_4^+$ adsorption process by TOCNBs, we performed tests using water samples containing 20 mg per L $K^+$, 20 mg per L $Ca^{2+}$, and 48 mg per L $SO_4^{2-}$—amounts within the ranges reported for wastewater and semi-industrial waters in physicochemical analyses.[16,79]

Fig. 5b shows how, at pH 7.0, cationic ($K^+$, $Ca^{2+}$) and anionic ($SO_4^{2-}$) species affect the ammonium adsorption capacity of the TOCNBs. The presence of coexisting monovalent cations, such as $K^+$, significantly reduces $NH_4^+$ adsorption on TOCNB. This is due to competitive interactions at the adsorption sites, where $K^+$ competes with $NH_4^+$ for binding to the negatively charged carboxylate ($-COO^-$) groups on the TOCNB surface.[16] However, the presence of divalent cations such as $Ca^{2+}$ exhibited a less pronounced inhibitory effect on $NH_4^+$ adsorption compared to monovalent cations like $K^+$. This behavior can be attributed to differences in the hydrated ionic radii of the competing cations in aqueous solution. The hydrated radius of $Ca^{2+}$ ($\approx$4.12 Å) is considerably larger than that of $NH_4^+$ ($\approx$3.31 Å), whereas $K^+$ ($\approx$3.31 Å) and $Na^+$ ($\approx$3.58 Å) exhibit similar values. The larger hydrated Ca ions are prevented from diffusing into and accessing the internal adsorption sites within the TOCN matrix by steric hindrance. Additionally, the higher charge density of $Ca^{2+}$ leads to stronger hydration, further reducing its mobility and affinity for exchange sites compared to $NH_4^+$. In contrast, $K^+$ may more readily interact with the negatively charged carboxylate groups ($-COO^-$), thereby displacing $NH_4^+$ more efficiently. Similar competitive ion-exchange behavior has been observed in zeolite-based adsorbents.[80] Additionally, the presence of

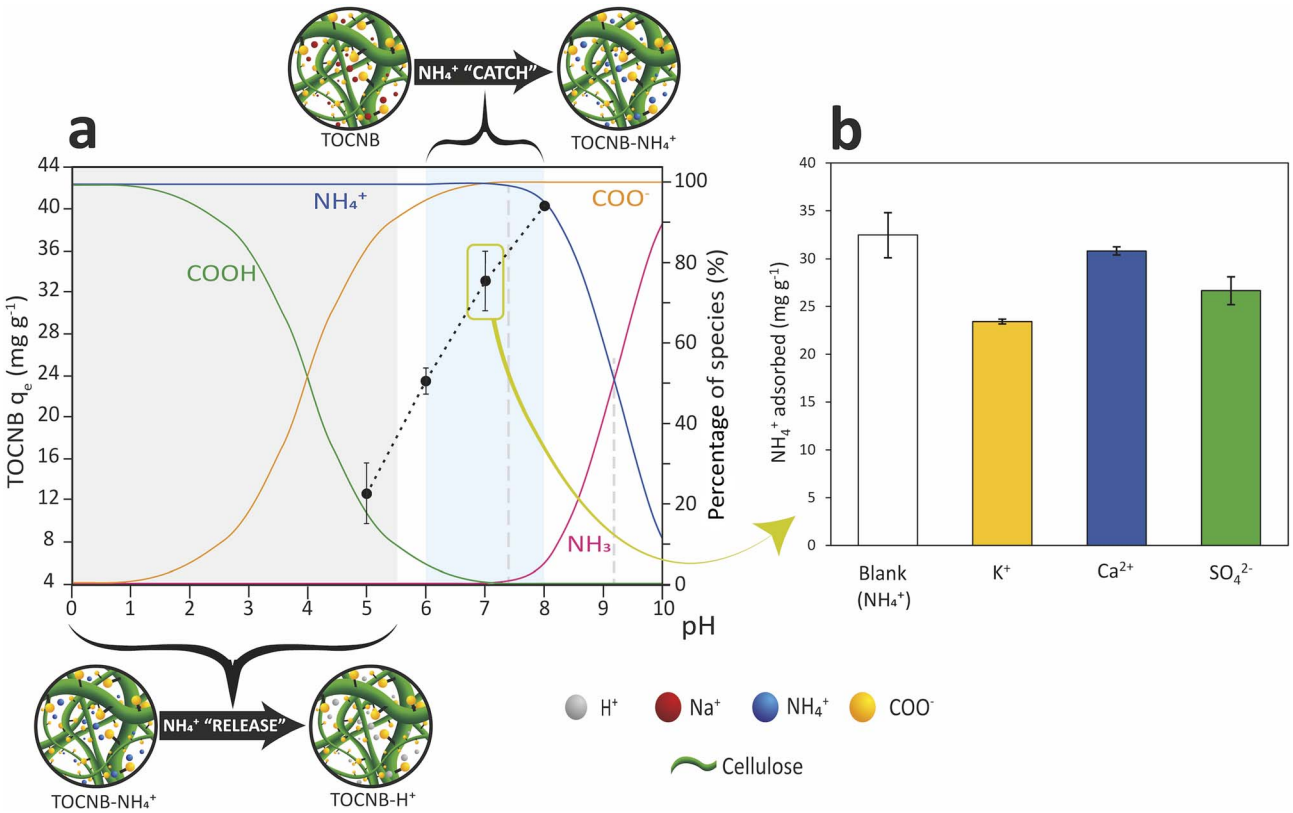


Fig. 5 (a) pH-dependent species (%) in TOCNB: protonated *vs.* deprotonated (green and yellow lines), ammonia: ammonium ion *vs.* ammonia (blue and pink lines), and TOCNB adsorption capacity of $NH_4^+$ at equilibrium ($q_e$, black dotted line). (b) Effect of ionic strength on the $NH_4^+$ adsorption capacity of TOCNB (100 mg per L $NH_4^+$, 20 mg per L $K^+$, 20 mg per L $Ca^{2+}$, and 48 mg per L $SO_4^{2-}$), TOCNB (0.25 g per L, pH 7.0, 60 min, 150 rpm at 20 °C).

divalent anions such as $SO_4^{2-}$ also reduces $NH_4^+$ uptake by TOCNBs. This effect is likely due to charge shielding and an increase in ionic strength, which compresses the electrical double layer around the active sites on the TOCNB surface, weakening electrostatic interactions between $NH_4^+$ and the adsorbent.[74,75] Despite these interferences, TOCN beads showed a high ability to "catch" ammonium in the model wastewater system, highlighting their robustness and suitability for future use in complex wastewater treatment matrices. The high variability observed in the $SO_4^{2-}$ is acknowledged as an experimental limitation of this study and suggests a behavior that requires further investigation in future work.

The effect of contact time on the ammonium adsorption capacity of TOCNB was systematically evaluated to elucidate the underlying adsorption kinetics. Two widely accepted models—the pseudo-first-order (PFO) and pseudo-second-order (PSO)—were applied to interpret the interaction dynamics between $NH_4^+$ ions and the carboxylated surface of the TOCNB hydrogel matrix.[81,82] The PFO model generally applies when physical processes, such as van der Waals forces, dominate adsorption. It assumes that the adsorption rate is proportional to the number of available sites, as shown in Fig. 6a. The non-linear form of this model can be written as:

$$q_t = q_e(1 - e^{-k_1 t}) \quad (3)$$

where $q_e$ and $q_t$ represent the amount of $NH_4^+$ (mg $g^{-1}$) adsorbed at equilibrium and at any time $t$ (min), respectively; $k_1$ represents the constant of the pseudo-first-order kinetics equation ($min^{-1}$). The PSO model is commonly used to describe adsorption, focusing on interactions between the adsorbate and the active sites on the adsorbent surface. It presumes that the adsorption rate depends on the square of the number of available active sites (see Fig. 6a). The nonlinear form of this model is expressed as:

$$q_t = \frac{q_e^2 k_2 t}{1 + q_e k_2 t} \quad (4)$$

where $q_e$ and $q_t$ represent the amount of $NH_4^+$ (mg $g^{-1}$) adsorbed at equilibrium and at any time $t$ (min), respectively; $k_2$ represents the constant of the pseudo-second-order kinetics equation (g $mg^{-1}$ $min^{-1}$).

As shown in Fig. 6a, the adsorption process displayed a biphasic pattern: a rapid initial phase within the first 30 minutes, followed by a plateau indicating saturation of active sites. The detailed fitting parameters for the two models, also presented in Fig. 6a, reveal a nuanced interplay between physical and electrostatic interactions. Although the PFO model provides a slightly better fit to the experimental data ($R^2$ = 0.9528) than the PSO model ($R^2$ = 0.9411), this does not preclude the involvement of electrostatic forces in the adsorption mechanism. A closer fit of the PFO model suggests that

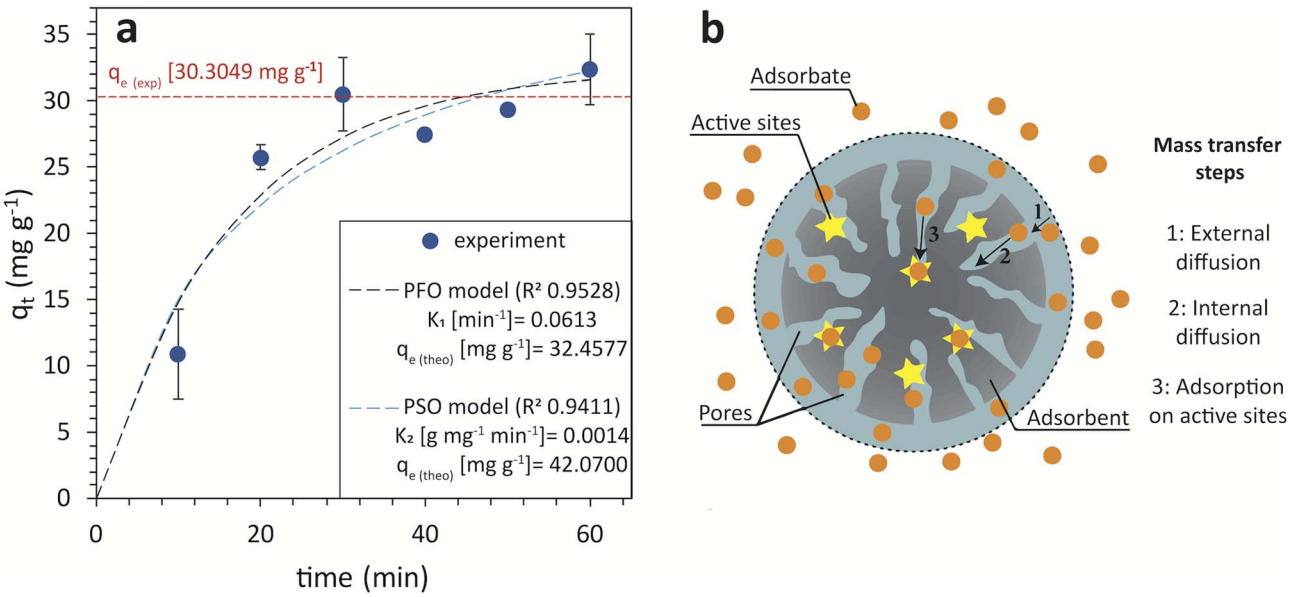


Fig. 6 (a) Experimental adsorption kinetics of $NH_4^+$ onto TOCNB (100 mg per L $NH_4^+$; 150 rpm; pH 7; 0.25 g per L TOCNB), showing rapid initial uptake followed by equilibrium saturation. The data are fitted to pseudo-first-order (PFO) and pseudo-second-order (PSO) kinetic models. (b) Schematics of possible $NH_4^+$/TOCNB interactions according to an adsorption mechanism governed by both physical diffusion and electrostatic interactions. The concept for this figure was inspired from Wang and Gou.[83]

physisorption processes, such as external and internal diffusion into the porous hydrogel matrix and weak van der Waals interactions, govern the rate-limiting step in $NH_4^+$ adsorption (Fig. 6b). This is consistent with the structural characteristics of TOCNB, which features a hydrated, highly porous network that facilitates rapid solute transport.

However, the PSO model, which assumes chemisorption through electrostatic forces or electron sharing, correlates with the affinity between the negatively charged carboxylate groups ($-COO^-$) on TOCNB and the cationic $NH_4^+$ species, as shown by the pH-driven adsorption capacity of the material reported earlier (Fig. 5). Previous studies on other cellulose-based adsorbents for cationic dyes and biomass-derived adsorbents for ammonium support the idea of a chemisorption process.[35,84] Additionally, the ionic-strength experiments confirm the importance of electrostatic interactions, as an increase in cation concentration reduces TOCNB adsorption capacity when such interactions are present, consistent with findings from other research teams.[16,35,85,86]

This apparent contradiction between physisorption and chemisorption can be reconciled by recognizing that adsorption likely proceeds through multiple sequential steps. Initially, $NH_4^+$ ions undergo rapid physical diffusion into the hydrogel matrix—a process well captured by the PFO model. Once inside, the ions interact with the carboxylate groups *via* electrostatic attraction, which governs the final adsorption capacity and is better described by the PSO model. Thus, the PFO model reflects the kinetic control of the early-stage adsorption process, while the PSO model captures the chemical affinity and equilibrium behavior of the system, as evidenced by enhanced $NH_4^+$ adsorption at higher pH and by the effect of ionic strength on TOCNB performance (Fig. 5). This duality shows the complex interplay between physical and electrostatic forces in the adsorption mechanism of TOCNB.

Adsorption isotherms provide quantitative parameters that describe surface capacity, affinity, and binding mechanisms, all of which are essential characteristics for establishing TOCNB performance. Fig. 7a shows how the adsorption capacity of $NH_4^+$ onto TOCNB ($q_e$) increases proportionally with the equilibrium concentration ($C_e$) up to approximately 100 mg $L^{-1}$. Beyond this threshold, the adsorption capacity plateaued, indicating saturation of the available active sites on the bead surface. To model the adsorption process, two well-established isotherm equations were applied: the Langmuir and Freundlich models. The Langmuir model assumes monolayer adsorption on a homogeneous surface with energetically equivalent sites and is described by the equation:[87]

$$q_e = \frac{q_m K_L C_e}{1 + K_L C_e} \quad (5)$$

In contrast, the Freundlich model accounts for adsorption on heterogeneous surfaces with varying site energies and is expressed as:[88]

$$q_e = K_F C_e^{\frac{1}{n}} \quad (6)$$

Here, $q_e$ is the equilibrium adsorption capacity (mg $NH_4^+$ per g), $C_e$ is the equilibrium concentration of $NH_4^+$ (mg $L^{-1}$), $q_m$ is the maximum monolayer adsorption capacity (mg $g^{-1}$), $K_L$ is the Langmuir adsorption constant (L $mg^{-1}$), and $K_F$ (L $g^{-1}$) and $n$ are the Freundlich constants representing adsorption capacity and intensity, respectively.

The isotherms parameters and correlation coefficients $R^2$ are shown in Fig. 7a. Nonlinear regression analysis of the

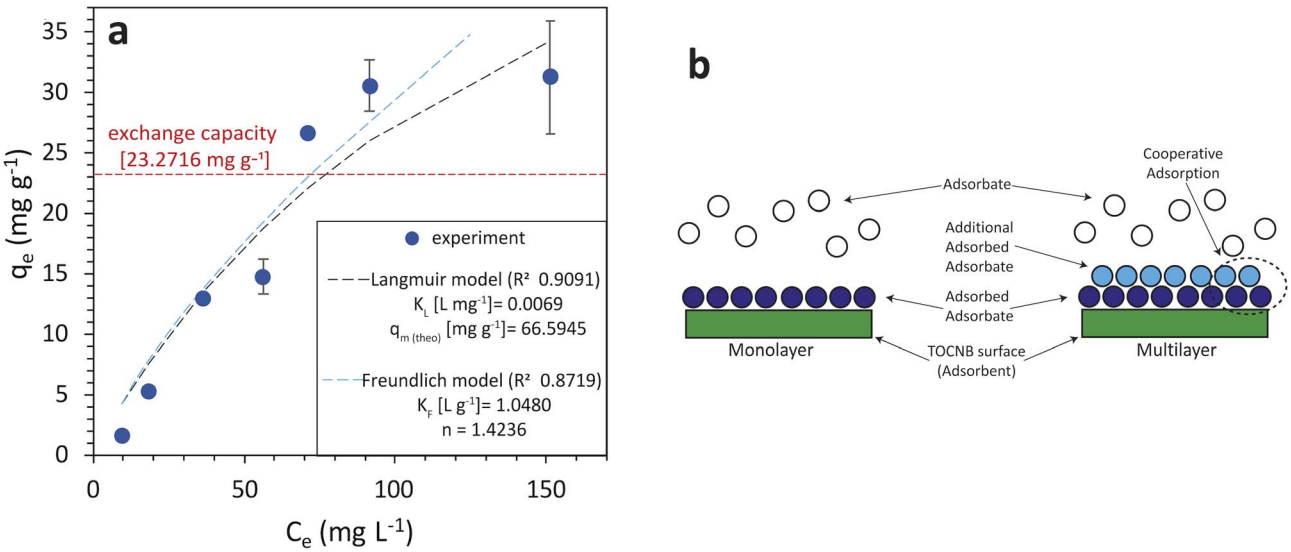


Fig. 7 (a) Experimental $NH_4^+$ adsorption isotherm onto TOCNB (100 mg per L $NH_4^+$; 150 rpm; pH 7; 0.25 g per L TOCNB). The data are fitted to Langmuir and Freundlich models. (b) Schematics of possible $NH_4^+$/TOCNB interactions *via* mono and multilayer formation. Own elaboration based on Nandiyanto *et al.*[93]

experimental data showed that the Langmuir model provided a superior fit ($R^2 = 0.9091$) compared to the Freundlich model ($R^2 = 0.8719$), suggesting that $NH_4^+$ adsorption onto TOCNB predominantly follows a monolayer mechanism. The Langmuir constant $K_L = 0.006$ and the Freundlich constant $n = 1.42$ both fall within ranges indicative of favourable adsorption conditions defined by $n$ ($1 < n < 10$) and $K_L$ ($0 < K_L < 1$). However, the slightly lower goodness-of-fit of the Freundlich model ($R^2 = 0.8719$) suggests residual heterogeneity in binding site energies or minor multilayer effects. Indeed, in many real hydrogel systems, not every adsorption site is chemically identical (due to differences in local polymer chain environment, accessibility, degree of substitution, or swelling). The Freundlich exponent ($n = 1.42$) close to unity suggests moderate heterogeneity or weak interactions beyond pure monolayer binding. Comparable observations have been made in modified hydrogels where hybrid behavior (Langmuir at high concentration, Freundlich at low) is reported.[14,89,90]

The structural characterization supports the mechanistic inference: the beads' interconnected three-dimensional porous network (as demonstrated in SEM images of Fig. 4) likely facilitates efficient ion diffusion into the interior and a relatively uniform exposure of functional groups throughout the hydrogel matrix. This morphology tends to reduce mass-transport limitations, making the adsorption more surface-limited (closer to ideal Langmuir behavior). In many cellulose-based adsorbents, achieving close-to-Langmuir behavior depends on good porosity and the accessibility of functional groups.[91]

Fig. 7a displays a red line indicating the theoretical cation adsorption capacity of TOCNB for $NH_4$, which is 23.27 mg $NH_4^+$ per g of TOCN. Assuming ammonium adsorption occurs through a stoichiometric interaction between the $-COO^-$ sites and $NH_4^+$ ions in a one-to-one manner, the TOCN with a carboxylate content ($\sigma$) of $1.29 \pm 0.08$ mmol $g^{-1}$ $mmol^{-1}$ $g^{-1}$ cellulose would adsorb an equal molar amount of $NH_4^+$—equivalent to $23.27 \pm 0.08$ mmol $g^{-1}$ $mg^{-1}$ $g^{-1}$ (calculated as 1.29 mmol $g^{-1}$ × 18.04 mg $mmol^{-1}$, the molar mass of ammonium). Experimentally, the adsorption capacity measured was 30.30 mg $NH_4^+$ per g, suggesting nearly complete saturation of the carboxylate sites. This supports the hypothesis that the density of carboxylate groups on the TOCNB also influences ammonium adsorption. Therefore, the adsorption efficiency of cellulose-based materials can be adjusted by controlling their oxidation degree, as also reported by Johnson *et al.*[92] for nitro-oxidized cellulose nanofibers (NO-CNF). These results confirm that the total number of carboxylate sites limits ammonium adsorption, validating the Langmuir isotherm model, which posits that each adsorption site interacts with one molecule. The slightly higher experimental capacity compared to the theoretical value suggests additional mechanisms—such as intraparticle diffusion or nonspecific interactions—that may also play a role, aligning with the kinetic studies. Confirming such contributions would require additional experiments—such as low-temperature adsorption studies—which are beyond the scope of the current study. Nonetheless, their involvement cannot be excluded.

The adsorption behavior of TOCNB resembles that of strong cation-exchange resins, where ammonium removal occurs through electrostatic interactions between $NH_4^+$ ions and negatively charged functional groups. Commercial sulfonated resins, such as Amberlite IR-120, Purolite C100, and Amberlyst 15 Wet, contain $-SO_3H$ groups that provide high ion-exchange capacity and strong selectivity toward ammonium, with reported values ranging from 25 to 70 mg $g^{-1}$ depending on operating conditions.[94–96] However, these synthetic resins require chemical regeneration using concentrated acids or salts, producing saline effluents and reducing process sustainability.[97] In contrast, TOCNB, which contains weak-acid $-COO^-$ groups, achieves a comparable adsorption capacity (30.30 mg $g^{-1}$) while being fully biodegradable.

Table 1 summarizes the ammonium adsorption capacities reported for conventional adsorbents, cellulose-based materials, and oxidized nanocellulose systems. Compared to other adsorbents for ammonium recovery, TOCNB combines competitive performance with clear sustainability advantages. As shown in Table 1, TOCNB achieves an ammonium adsorption capacity of 30.30 mg $g^{-1}$, comparable to conventional materials such as zeolites (12–35 mg $g^{-1}$) and higher than other nanocellulose-based systems, including TEMPO-oxidized nanofibers (13 mg $g^{-1}$). Beyond performance, TOCN beads are biodegradable, derived from residual biomass, and prepared without organic crosslinking agents, aligning with circular economy principles. The beads' hydrogel architecture provides a porous, hydrated network that promotes ammonium diffusion, enhances effective adsorption, and also contributes to water retention when applied to soils. At the same time, the TOCNB's pH-responsive behavior enables ammonium capture under typical wastewater conditions and controlled release in acidic soils. These features position TOCNB as a sustainable and multifunctional alternative to conventional adsorbents.

Cellulose-based adsorbents exhibit a strong dependence on chemical functionalization for ammonium adsorption. Unmodified cellulose shows negligible ammonium adsorption (<5 mg $g^{-1}$), whereas chemical modifications such as etherification with glycidyl trimethyl ammonium chloride (GTMAC) or sulfonation with chlorosulfonic acid markedly improve performance up to 40.38 mg $g^{-1}$.[74,92] In contrast, TOCNB achieves comparable adsorption capacity (30.30 mg $g^{-1}$) without incorporating additional functional components into the macrostructure, thereby simplifying material composition and reducing processing steps.

Studies on oxidized cellulose materials as ammonium adsorbents remain limited, and, to the best of our knowledge, none have reported the preparation of hydrogel beads *via* ionotropic gelation with salts for that purpose. Nitro-oxidized cellulose nanofibers (NO-CNF) and TEMPO-oxidized nanocellulose (TOCN) have been investigated, but adsorption was not their primary focus. Despite similar oxidation degrees ($\approx$1.29 mmol $g^{-1}$), both NO-CNF and TOCN exhibit lower adsorption capacities than TOCNB, suggesting that bead architecture and hydrogel network formation enhance ammonium binding. TEMPO-oxidized microcrystalline cellulose (TOC) shows even lower performance, with capacities approximately three times lower than those achieved in this work. The adsorption capacity of TOCNB we report, 30.30 mg $g^{-1}$, ranks among the highest reported for oxidized cellulose systems, positioning TOCNB as a competitive bio-based adsorbent for ammonium recovery.

On the other hand, the ammonium-loaded TOCN beads were designed for direct reuse rather than chemical regeneration, as demonstrated in the following section. The beads, synthesized from residual palm-oil biomass, provide a biodegradable and low-cost cellulose matrix that adsorbs ammonium from wastewater. Instead of undergoing additional regeneration steps after ammonium "catch" from wastewater, TOCNB can be recovered and incorporated into soil as a biodegradable controlled-release nitrogen fertilizer, which can also supply organic carbon from the cellulosic matrix. This approach eliminates chemical treatments and integrates ion exchange, nutrient recovery, and agricultural reuse into a single, sustainable system that aligns with circular economy principles.

### 3.3 Germination tests

To evaluate the potential of TOCNB–$NH_4^+$ as a fertilizer, a simple germination and growth experiment was conducted using red beans (*Phaseolus vulgaris*) under three soil treatments: S1 (sand control), S2 (sand with TOCNB–$NH_4^+$), and S3 (sand with urea). Over two weeks, stem length, dry biomass, leaf

Table 1 $q_e$ values for different ammonium adsorption materials

| | $q_e$ (mg $NH_4^+$ per g) | Reference |
|---|---|---|
| **Conventional adsorbents** | | |
| Natural zeolite | 20.94 | Liu *et al.*[98] |
| Synthetic/modified zeolites | 12–35 | Junyuan *et al.*[99] He *et al.*[100] |
| Activated carbon | 1–24 | Safie *et al.*[101] Sahu *et al.*[102] |
| Biochar (modified) | 1–53 | Mohamed *et al.*[103] Nguyen *et al.*[104] |
| Other clays (Bentonite, Kaolin) | 8–17 | Truong *et al.*[105] Zaini *et al.*[106] |
| **Cellulose-based materials** | | |
| Unmodified cellulose fibers | <5 | Gupta *et al.*[107] |
| Amphoteric cellulose (GTMAC etherified) | 40.38 | Zhang *et al.*[74] |
| Sulfonated CNF (CSNF) | 35.1 | Johnson *et al.*[108] |
| **Oxidized cellulose-based materials** | | |
| Nitro-oxidized cellulose nanofiber (NO-CNF), $\sigma = 1.1$ mmol $g^{-1}$ | 22.7 | Johnson *et al.*[92] |
| TEMPO-oxidized cellulose nanofibers (TOCNFs), $\sigma = 1.2$ mmol $g^{-1}$ | 13 | Johnson *et al.*[92] |
| TEMPO-oxidized microcrystalline cellulose (TOC), $\sigma = 0.78$ mmol $g^{-1}$ | 8.21 | Ong *et al.*[109] |
| TEMPO-oxidized cellulose nanofiber beads (TOCNBs), $\sigma = 1.29$ mmol $g^{-1}$ | 30.30 | This work |

number, and leaf length were monitored to assess the impact of each treatment on plant development. The analysis of leaf length was conducted on trifoliate leaves, which are considered the true leaves in plant biology, as the primary leaves—cotyledons—serve mainly as nutrient sources derived from the seed.[110]

The results in Fig. 8 revealed that both TOCNB–$NH_4^+$ and urea significantly enhanced plant growth compared to the control. This improvement can be attributed to the exogenous nitrogen from TOCNB-$NH_4^+$ or the commercial fertilizer.[111,112] During the first week, stem elongation was more pronounced in the TOCNB–$NH_4^+$ treatment, suggesting an early release of ammonium from the beads. However, by day 15, plants treated with urea exhibited greater stem length, although the error bars suggest no statistical difference between the TOCNB–$NH_4^+$ and urea. Interestingly, despite the longer stems observed in the urea treatment, the TOCNB–$NH_4^+$ group produced higher dry biomass after 2 weeks, indicating more compact, structurally robust growth. This suggests that the controlled release of nutrients from TOCNB beads supports balanced development rather than excessive elongation. Leaf development followed a similar trend. Both TOCNB–$NH_4^+$ and urea treatments resulted in more leaves and trifoliate leaf formation than the control, confirming the positive effect of nitrogen supplementation.

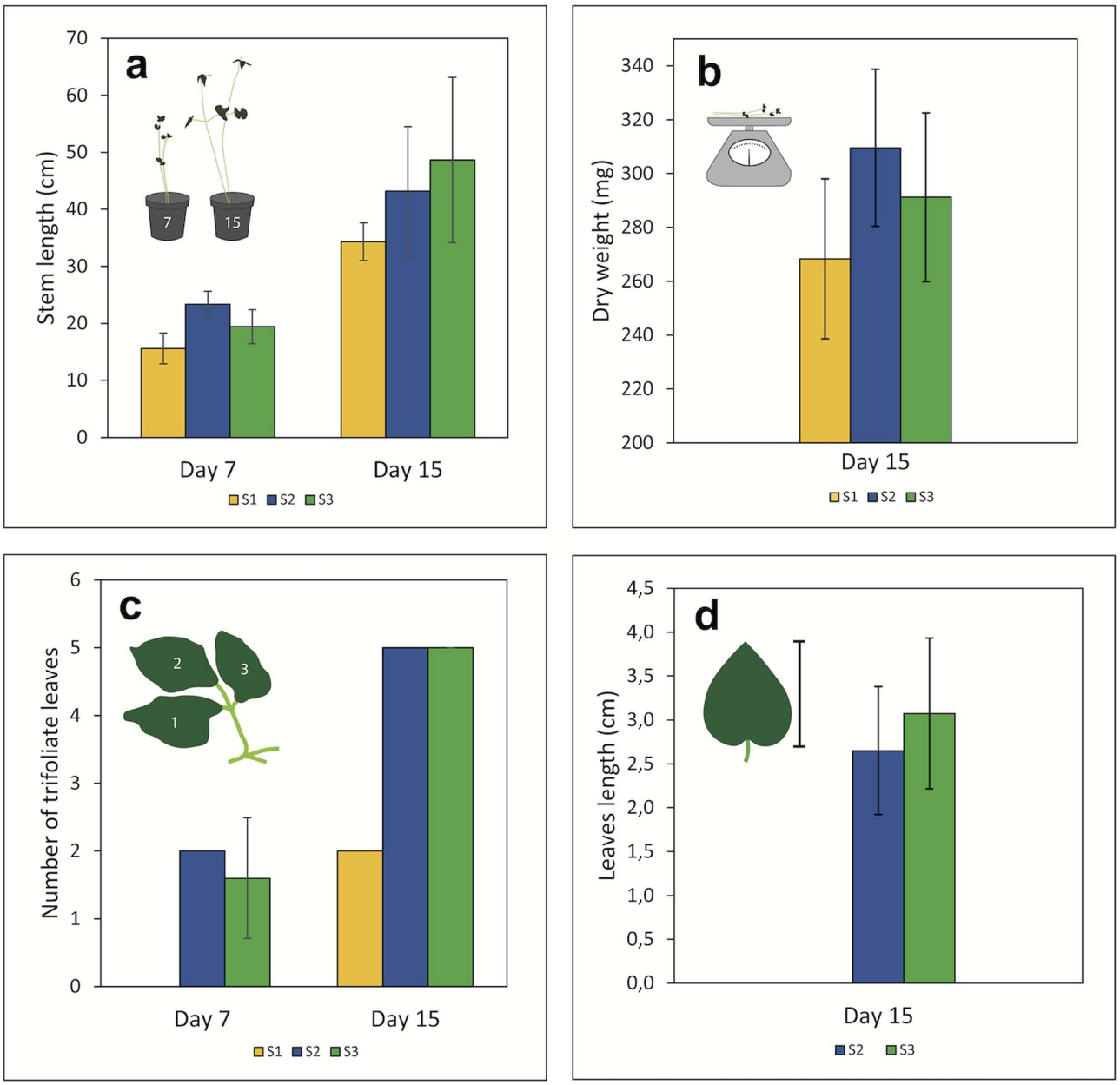


Fig. 8 Germination and growth performance of *Phaseolus vulgaris* L. seeds under three soil treatments over two weeks: S1 – control (quartz sand only), S2 – quartz sand mixed with TOCNB–$NH_4^+$ (ammonium adsorbed onto TEMPO-oxidized cellulose nanofiber beads), and S3 – quartz sand mixed with urea (commercial fertilizer). Growth parameters measured include (a) stem length, (b) total number of leaves, (c) number of trifoliate leaves, and (d) average leaf length.

While urea promoted more rapid leaf elongation, TOCNB–$NH_4^+$ provided a steady increase in leaf size, reflecting a gradual nutrient release that supports sustained foliar growth.

Overall, the performance of TOCNB–$NH_4^+$ was comparable to that of commercial urea fertilizer. Its ability to gradually release ammonium makes it particularly suitable for acidic soils, where nutrient retention and controlled availability are critical. These findings highlight the technical feasibility of using TOCNB beads as a sustainable biofertilizer derived from agricultural waste, aligning with circular economy principles and offering promising applications in eco-friendly agriculture.[36]

# 4 Conclusions

This study demonstrates the successful synthesis and multifunctional performance of TEMPO-oxidized cellulose nanofiber beads (TOCNB) derived from palm oil empty fruit bunches (EFB), a lignocellulosic agricultural residue. The beads were fabricated *via* a one-step TEMPO-mediated oxidation followed by sodium-ion-induced external ionotropic gelation, yielding hydrogel structures with high porosity, mechanical stability, and swelling capacity.

TOCNBs exhibited a notable ammonium adsorption capacity of 30.30 mg per g $NH_4^+$, with adsorption behavior governed by physisorption and electrostatic interactions between carboxylate groups and ammonium ions. Adsorption kinetics followed a pseudo-first-order model, while equilibrium data were best described by the Langmuir isotherm, indicating a monolayer adsorption mechanism. The adsorption efficiency was significantly influenced by pH, ionic strength, and contact time, with optimal performance observed at pH 6–8 and equilibrium reached within 60 minutes.

Notably, the beads demonstrated controlled nutrient release in model soils (quartz sand), as evidenced by germination assays with *Phaseolus vulgaris* L. seeds, in which TOCNB–$NH_4^+$ treatments promoted seedling growth comparable to that of commercial urea fertilizers. The gradual release of ammonium from TOCNBs supported balanced biomass accumulation and foliar development, showing their potential as biodegradable, slow-release fertilizers.

Overall, TOCNBs represent a sustainable and circular solution for nutrient recovery from wastewater and reuse in agriculture. Their dual functionality as adsorbents and biofertilizers, combined with their renewable biomass origin, positions them as promising candidates for eco-friendly water treatment and soil amendment applications.

# Author contributions

Y. R.-T.: methodology, data acquisition, processing and analysis, interpretation, investigation, validation, writing – original draft. L. A. C.-V.: conceptualization, supervision, editing. C. B. T.: funding acquisition, project administration, supervision. M. Y. C.: conceptualization, methodology, data acquisition, processing and analysis, interpretation, supervision, visualization, resources, funding acquisition, project administration, writing – review & editing.

# Conflicts of interest

The authors declare that they have no known competing financial interests or personal relationships that could have influenced the work reported in this paper.

# Data availability

The data supporting this article have been included as part of the supplementary information (SI). Supplementary information: TOCNBs characterization (oxidation degree and carboxylate content calculated from conductimetric titrations, along with IR-ATR spectra, zeta potential data, and bead mass). Adsorption data ($NH_4^+$ adsorption capacity – $q_e$ – changes with pH, effects of ions on adsorption, experimental kinetics, and isotherm data). Agricultural results (data from a two-week growth performance of *Phaseolus vulgaris* L seeds using three soil treatments, including plant metrics like stem length, dry weight, and number/length of leaves). See DOI: https://doi.org/10.1039/d5ra08174b.

# Acknowledgements

The authors acknowledge the Guatiguará Technology Park and the Central Research Laboratory Facility at Universidad Industrial de Santander (UIS) for infrastructural support. We also acknowledge financial support from the SGR-Gobernación de Santander Grant BPIN 2021000100536. During the preparation of this work, the authors used Grammarly Editor v1.120.0.0 and OpenAI's ChatGPT to improve language and clarity during manuscript drafting. After using these tools, the authors reviewed and edited the text as needed. All intellectual content and conclusions are the authors' own.

# Notes and references

1 C. Liyanage and K. Yamada, *Sustainability*, 2017, **9**, 1405, DOI: 10.3390/su9081405.
2 Food and Agriculture Organization of the United Nations (FAO), *World Fertilizer Trends and Outlook to 2022*, FAO, Rome, 2019.
3 M. Farghali, Z. Chen, A. I. Osman, I. M. Ali, D. Hassan, I. Ihara, D. W. Rooney and P. Yap, *Environ. Chem. Lett.*, 2024, **22**, 2699–2751.
4 T. Zhou, M. Wang, H. Zeng, R. Min, J. Wang and G. Zhang, *Environ. Geochem. Health*, 2024, **46**, 344.
5 Y. Ye, H. Ngo, W. Guo, Y. Liu, S. Woong, D. D. Nguyen, H. Liang and J. Wang, *Bioresour. Technol.*, 2018, **268**, 749–758.
6 S. Brunauer, P. H. Emmett and E. Teller, *J. Am. Chem. Soc.*, 1938, **60**, 309–319.
7 K. Y. Foo and B. H. Hameed, *Chem. Eng. J.*, 2010, **156**, 2–10.
8 M. A. Hubbe, S. Park and S. J. Park, *Bioresources*, 2012, **7**, 3108–3151.
9 J. Huang, K. Rathnayake, C. Chow, D. Welsh, T. Li and P. Teasdale, *J. Environ. Sci.*, 2018, **63**, 174–197.

10 X. Xing, W. Li, J. Zhang, H. Wu, Y. Guan and H. Gao, *Cellulose*, 2021, **28**, 7953–7968.
11 C. Poornachandhra, R. Jayabalakrishnan, M. Prasanthrajan, G. Balasubramanian, A. Lakshmanan, S. Selvakumar and J. John, *RSC Adv.*, 2023, **13**, 4757–4774.
12 R. Song, E. Zhu, R. Hou, J. Bao, D. Chen, Z. Shi, Q. Yang and C. Xiong, *Cellulose*, 2024, **31**, 5077–5095.
13 Q. Wang, S. Liu, H. Chen, J. Liu, H. Liu and Q. Zhu, *BioResources*, 2023, **18**, 4104–4115.
14 Y. Zheng, Y. Xie and A. Wang, *Chem. Eng. J.*, 2012, **179**, 90–98.
15 B. Shahrooie, L. Rajabi, A. A. Derakhshan and M. Keyhani, *J. Taiwan Inst. Chem. Eng.*, 2015, **51**, 201–215.
16 X. Wang, S. Lü, C. Gao, X. Xu, X. Zhang, X. Bai, M. Liu and L. Wu, *Chem. Eng. J.*, 2014, **252**, 404–414.
17 A. Abdulrazik, M. Elsholkami, A. Elkamel and L. Simon, *J. Cleaner Prod.*, 2017, **168**, 131–148.
18 F. N. Mohammad Padzil, S. H. Lee, Z. M. A. ari Ainun, C. H. Lee and L. C. Abdullah, *Materials*, 2020, **13**, 1–26.
19 T. S. Hamidon, R. Adnan, M. K. Mohamad Haafiz and M. H. Hussin, *Environ. Chem. Lett.*, 2022, **20**, 1965–2017.
20 H. Fukuzumi, R. Tanaka, T. Saito and A. Isogai, *Cellulose*, 2014, **21**, 1553–1559.
21 A. Isogai, T. Saito and H. Fukuzumi, *Nanoscale*, 2011, **3**, 71–85.
22 K. J. De France, T. Hoare and E. D. Cranston, *Chem. Mater.*, 2017, **29**, 4609–4631.
23 H. Dong, J. F. Snyder, K. S. Williams and J. W. Andzelm, *Biomacromolecules*, 2013, **14**, 3338–3345.
24 M. Pavelková, K. Kubová, J. Vysloužil, *et al.*, *AAPS PharmSciTech*, 2017, **18**, 1343–1354.
25 M. Chau, S. E. Sriskandha, D. Pichugin, H. Thérien-Aubin, D. Nykypanchuk, G. Chauve, M. Méthot, J. Bouchard, O. Gang and E. Kumacheva, *Biomacromolecules*, 2015, **16**, 2455–2462.
26 L. Mendoza, W. Batchelor, R. F. Tabor and G. Garnier, *J. Colloid Interface Sci.*, 2018, **509**, 39–46.
27 M. Gericke, J. Trygg and P. Fardim, *Chem. Rev.*, 2013, **113**, 4812–4836.
28 Y. Morimoto, N. Tsukida, H. Saga and H. Saito, *US Pat.*, 5972507, 1999.
29 L. Zhang, J. Zhou, L. Zhang, Y. Wang, H. Chen and Y. Du, *Carbohydr. Polym.*, 2005, **61**, 447–452.
30 B. Schroeter, V. P. Yonkova, N. A. M. Niemeyer, I. Jung, I. Preibisch, P. Gurikov and I. Smirnova, *Cellulose*, 2021, **28**, 223–239.
31 C. Callaghan, J. L. Scott, K. J. Edler and D. Mattia, *J. Colloid Interface Sci.*, 2022, **627**, 1003–1010.
32 R. A. de Carvalho, G. Veronese, A. J. F. Carvalho, E. Barbu, A. C. Amaral and E. Trovatti, *Cellulose*, 2016, **23**, 3399–3405.
33 Y. Tian, Y. Kong, X. Liu, L. Chen, L. Wang, L. Zhou, G. Wang and Q. Zhang, *Carbohydr. Polym.*, 2025, **348**, 122848.
34 J. Xue, E. Zhu, H. Zhu, D. Liu, H. Cai, C. Xiong, Q. Yang and Z. Shi, *Cellulose*, 2023, **30**, 1623–1636.
35 S. Liu, G. Cheng, Y. Xiong, Y. Ding and X. Luo, *J. Hazard. Mater.*, 2020, **384**, 121195.
36 B.-E. Channab, A. El Idrissi, Y. Essamlali and M. Zahouily, *J. Environ. Manage.*, 2024, **349**, 119928.
37 S. A. Ovalle-Serrano, C. Blanco-Tirado and M. Y. Combariza, *Cellulose*, 2018, **25**, 151–165.
38 A. Martínez-Ramírez, S. Rincón-Ortiz, V. Baldovino-Medrano and C. Blanco-Tirado, *RSC Adv.*, 2023, **13**, 36117–36129.
39 J. Trygg, P. Fardim, M. Gericke, E. Mäkilä and J. Salonen, *Carbohydr. Polym.*, 2013, **93**, 291–299.
40 K. Pal and I. Banerjee, in *Polymeric Gels – Characterization, Properties and Biomedical Applications*, Elsevier, 2018, p. 2.
41 R. Rohaizu and W. D. Wanrosli, *Ultrason. Sonochem.*, 2017, **34**, 631–639.
42 J. Levanič, K. Svedström, V. Liljeström, M. Šernek, I. G. Osojnik Črnivec, N. Poklar Ulrih and A. Haapala, *Cellulose*, 2022, **29**, 9121–9142.
43 R. Kuramae, T. Saito and A. Isogai, *React. Funct. Polym.*, 2014, **85**, 126–133.
44 A. B. Fall, S. B. Lindström, O. Sundman, L. Ödberg and L. Wågberg, *Langmuir*, 2011, **27**, 11332–11338.
45 R. Wicaksono, K. Syamsu, I. Yuliasih and M. Nasir, *Chem. Mater. Res.*, 2013, **3**, 79–87.
46 L. A. Calderón-Vergara, S. A. Ovalle-Serrano, C. Blanco-Tirado and M. Y. Combariza, *Cellulose*, 2020, **27**, 1273–1288.
47 E. Pretsch, P. Bühlmann and M. Badertscher, *Structure Determination of Organic Compounds: Tables of Spectral Data*, Springer Berlin Heidelberg, 4th edn, 2009.
48 E. Abraham, B. Deepa, L. A. Pothan, M. Jacob, S. Thomas, U. Cvelbar and R. Anandjiwala, *Carbohydr. Polym.*, 2011, **86**, 1468–1475.
49 G. Ramadoss and K. Muthukumar, *Biochem. Eng. J.*, 2014, **83**, 33–41.
50 K. Chuensangjun, T. Kanomata, Y. Kitaoka, Y. Chisti and S. Sirisansaneeyakul, *J. Polym. Environ.*, 2019, **27**, 847–861.
51 N. Masruchin, B. D. Park, V. Causin and I. C. Um, *Cellulose*, 2015, **22**, 1993–2010.
52 D. Ishii, T. Saito and A. Isogai, *Biomacromolecules*, 2011, **12**, 548–550.
53 A. Rossetti, A. Paciaroni, B. Rossi, C. Bottari, L. Comez, S. Corezzi and A. Fiorati, *Cellulose*, 2023, **30**, 2951–2967.
54 M. Suneetha, H. Kim and S. S. Han, *Int. J. Biol. Macromol.*, 2024, **256**, 128364.
55 A. Sattari, A. Basirattalab and I. Alemzadeh, *Can. J. Chem. Eng.*, 2025, **103**, 3521–3530.
56 N. Masruchin, B. D. Park and V. Causin, *Cellulose*, 2018, **25**, 485–502.
57 J. C. Russ, *The Image Processing Handbook*, CRC Press, Boca Raton, 5th edn, 2006.
58 S. Ramanujan, *Q. J. Math.*, 1914, **45**, 350–372.
59 M. Landreau, H. You, D. A. Stahl and M. K. H. Winkler, *npj Clean Water*, 2021, **4**, 43.
60 F. Lin, Y. You, X. Yang, X. Jiang, Q. Lu, T. Wang, B. Huang and B. Lu, *Cellulose*, 2017, **24**, 5025–5040.
61 G. D. Nicodemus and S. J. Bryant, *J. Biomech.*, 2008, **41**, 1528–1536.

62 H. Li and V. Silberschmidt, in *The Mechanics of Hydrogels: Mechanical Properties, Testing, and Applications*, ed. J. Hu, Elsevier, Amsterdam, 2022, pp. 1–24.
63 L. Berglund, F. Forsberg, M. Jonoobi and K. Oksman, *RSC Adv.*, 2018, **8**, 38219–38228.
64 K. Y. Lee and D. J. Mooney, *Prog. Polym. Sci.*, 2012, **37**, 106–126.
65 K. Kabiri, H. Omidian, S. A. Hashemi and M. J. Zohuriaan-Mehr, *Eur. Polym. J.*, 2003, **39**, 1341–1348.
66 L. Zhu, V. Kumar and G. S. Banker, *AAPS PharmSciTech*, 2004, **5**, 69.
67 M. Spaic, D. P. Small, J. R. Cook and W. Wang, *Cellulose*, 2014, **21**, 1529–1540.
68 K. M. Z. Hossain, V. Calabrese, M. A. da Silva, S. J. Bryant, J. Schmitt, J. H. Ahn-Jarvis, F. J. Warren, Y. Z. Khimyak, J. L. Scott and K. J. Edler, *Polymers*, 2021, **13**, 951, DOI: 10.3390/polym13060951.
69 P. Liu, K. Oksman and A. P. Mathew, *J. Colloid Interface Sci.*, 2016, **464**, 175–182.
70 W. M. Haynes, *CRC Handbook of Chemistry and Physics*, CRC Press, Boca Raton, 97th edn, 2016.
71 EMPAS S.A., *Especificaciones Técnicas Operación PTAR Río Frío*, EMPAS S.A., Bucaramanga, 2021, available at https://www.empas.gov.co/wp-content/uploads/2021/04/ESPECIFICACIONES-TECNICAS-OPERACION-PTAR-V.2.pdf.
72 M. B. Pescod, *Wastewater Treatment and Use in Agriculture*, FAO Irrigation and Drainage Paper No. 47, Food and Agriculture Organization of the United Nations, Rome, 1992.
73 Ministry of Environment and Sustainable Development, Resolution 631 of 2015: Establishing the parameters and maximum permissible limit values for specific discharges into surface water bodies and public sewage systems and issuing other provisions, Bogotá, Official Gazette No. 49,486, 2015.
74 T. Zhang, Y. Sun, H. Li, M. Niu, Y. Guo, J. Zhou and F. Zhang, *Eur. Polym. J.*, 2022, **171**, 111223.
75 X. Wang, S. Lü, C. Gao, C. Feng, X. Xu, X. Bai, N. Gao, J. Yang, M. Liu and L. Wu, *ACS Sustainable Chem. Eng.*, 2016, **4**, 2068–2079.
76 Instituto de Investigación de Recursos Biológicos Alexander von Humboldt, Emisiones de CO2 por la aplicación de cal en suelos ácidos en Colombia, 2021, available at: https://biocarbono.org/wp-content/uploads/2021/09/02-emisiones-co2-por-aplicacion-cal-suelos-acidos-colombia.pdf.
77 S. F. Trelease and H. M. Trelease, *Am. J. Bot.*, 1935, **22**, 520–542.
78 G. H. Bolt, M. G. M. Bruggenwert and A. Kamphorst, in *Soil Chemistry: A. Basic Elements*, ed. G. H. Bolt and M. G. M. Bruggenwert, Elsevier, 1976, vol. 5, ch. 4, pp. 54–90.
79 J. L. Esquivel and M. Lacayo, *Rev. Torreón Univ.*, 2020, **9**, 58–76.
80 K. Yang, X. Zhang, C. Chao, B. Zhang and J. Liu, *Carbohydr. Polym.*, 2014, **107**, 103–109.
81 S. Lagergren, *K. Sven. Vetenskapsakad. Handl.*, 1898, **24**, 1–39.
82 Y. S. Ho and G. McKay, *Process Biochem.*, 1999, **34**, 451–465.
83 J. Wang and X. Guo, *J. Hazard. Mater.*, 2020, 122156, DOI: 10.1016/j.jhazmat.2020.122156.
84 Z. Ma, Q. Li, Q. Yue, B. Gao, W. Li, X. Xu and Q. Zhong, *Chem. Eng. J.*, 2011, **171**, 1209–1217.
85 Y. Zheng and A. Wang, *Chem. Eng. J.*, 2011, **171**, 1201–1208.
86 H. J. Hong, J. S. Lim, J. Y. Hwang, M. Kim, H. S. Jeong and M. S. Park, *Carbohydr. Polym.*, 2018, **195**, 136–142.
87 I. Langmuir, *J. Am. Chem. Soc.*, 1918, **40**, 1361–1403.
88 H. M. F. Freundlich, *Z. Phys. Chem.*, 1906, **57**, 385–470.
89 J. Lehtonen, J. Hassinen, A. A. Kumar, L.-S. Johansson, R. Mäenpää, N. Pahimanolis, T. Pradeep, O. Ikkala and O. J. Rojas, *Cellulose*, 2020, **27**, 10719–10732.
90 T. Tasić, V. Milanković, C. Unterweger, C. Fürst, S. Breitenbach, I. A. Pašti and T. Lazarević-Pašti, *C*, 2024, **10**, 58, DOI: 10.3390/c10030058.
91 A. El Mahdaoui, S. Radi, A. Elidrissi, M. A. F. Faustino, M. G. P. M. S. Neves and N. M. M. Moura, *J. Environ. Chem. Eng.*, 2024, **12**, 113870.
92 K. I. Johnson, G. Ilacas, R. Das, H.-Y. Chang, P. R. Sharma, C. O. Dimkpa and B. S. Hsiao, *Sustainability Sci. Technol.*, 2024, **1**, 14001.
93 A. B. D. Nandiyanto, R. Maryanti, M. Fiandini, R. Ragadhita, D. Usdiyana, S. Anggraeni, W. R. Arwa and A. Sh. M. Al-Obaidi, *Molekul*, 2020, **15**, 199–209.
94 A. Malovanyy, H. Sakalova, Y. Yatchyshyn, E. Plaza and M. Malovanyy, *Desalination*, 2013, **329**, 93–102.
95 S. Sadeghi, M. Abbasi, S. Osfouri, M. J. Dianat and J. Khodaveisi, *Membr. Water Treat.*, 2021, **12**, 271–284.
96 C. N. Vignoli, J. M. C. F. Bahé and M. R. C. Marques, *Polym. Bull.*, 2015, **72**, 3119–3134.
97 W. A. Tarpeh, C. N. Barazesh, M. R. Cath and K. L. Nelson, *Environ. Sci.: Water Res. Technol.*, 2018, **4**, 828–838.
98 P. Liu, A. Zhang, Y. Liu, Z. Liu, X. Liu, L. Yang and Z. Yang, *Water*, 2022, **14**, 2413, DOI: 10.3390/w14152413.
99 L. H. Junyuan, W. Qian, L. Li, Z. Changwu and W. Zhuo, *Chin. J. Environ. Eng.*, 2015, **9**, 4903–4909.
100 H. He, F. Gong, K. Fang, F. Peng and K. Wang, *J. Environ. Sci.*, 2019, **85**, 177–188.
101 N. N. Safie, A. Y. Zahrim, M. Rajin, N. M. Ismail, S. Saalah, S. M. Anisuzzaman and T. T. H. Calvin, *IOP Conf. Ser.: Mater. Sci. Eng.*, 2019, **606**, 012003, DOI: 10.1088/1757-899X/606/1/012003.
102 J. N. Sahu, F. Dhaouadi, L. Sellaoui, L. X. Khor, S. Y. Lee, W. M. A. W. Daud and A. B. Lamine, *Environ. Sci. Pollut. Res.*, 2024, **31**, 27980–27987.
103 N. B. Mohamed, N. Ngadi, A. I. Rushdan, N. Y. Yahya, M. H. Mohamed Noor, I. M. Inuwa and N. Ali, *ChemNanoMat*, 2025, **11**, e202400539, DOI: 10.1002/cnma.202400539.
104 L. H. Nguyen, V. P. Kha and N. Van Thai, *Environ. Geochem. Health*, 2024, **46**, 474, DOI: 10.1007/s10653-024-02210-2.
105 M. T. Truong, T. M. Pham and T. H. Dang, *Studying Livestock Breeding Wastewater Treatment with Bentonite Adsorbent*, 2018.

106 N. S. M. Zaini, I. W. Lenggoro, M. N. Naim, N. Yoshida, H. C. Man, N. F. A. Bakar and S. W. Puasa, *Adv. Powder Technol.*, 2021, **32**, 1833–1843.
107 V. K. Gupta, P. J. M. Carrott, R. Singh, M. Chaudhary and S. Kushwaha, *Bioresour. Technol.*, 2016, **216**, 1066–1076.
108 K. I. Johnson, W. Borges, P. R. Sharma, S. K. Sharma, H.-Y. Chang, M. M. Abou-Krisha and B. S. Hsiao, *Nanomaterials*, 2024, **14**, 507, DOI: 10.3390/nano14060507.
109 J. H. Ong, Y. N. Liang, X. Hu and R. Xu, *Ind. Eng. Chem. Res.*, 2022, **61**, 7665–7673.
110 C. Lopes, P. Fevereiro and S. de Sousa Araújo, *Front. Plant Sci.*, 2025, **16**, 1597915.
111 D. B. Basnet, K. B. Basnet and P. Acharya, *Int. J. Appl. Sci. Biotechnol.*, 2022, **10**, 31–40.
112 M. A. Youssef, A. F. Yousef, M. M. Ali, A. I. Ahmed, S. F. Lamlom, W. R. Strobel and H. M. Kalaji, *AMB Express*, 2021, **11**, 133.